RSC Advances

PAPER

View Article Online
View Journal | View Issue

Cite this: *RSC Adv.*, 2017, **7**, 23319

One-step synthesis of band-tunable N, S co-doped commercial TiO_2/graphene quantum dots composites with enhanced photocatalytic activity†

Kai Shen,[a] Xin Xue,[b] Xiaoyi Wang,[e] Xiaoying Hu,[d] Hongwei Tian *[a] and Weitao Zheng [ac]

N, S co-doped commercial TiO_2/N, S-GQDs graphene quantum dots (NSTG) composites with band tunability are synthesized *via* a facile solvothermal treatment in the presence of thiourea, which acts as a precursor for the dopants. The as prepared nanocomposites are characterized *via* X-ray diffraction (XRD), Raman spectroscopy (Raman), scanning electron microscopy (SEM), transmission electron microscopy (TEM), X-ray photoelectron spectroscopy (XPS), Fourier transform-infrared spectroscopy (FT-IR) and UV-vis diffuse reflectance spectroscopy (UV-vis DRS). The photocatalytic activity of NSTG is evaluated through the degradation of methylene blue (MB) under visible light irradiation (λ > 400 nm). Compared with commercial TiO_2 (P25) and N, S co-doped TiO_2 (NST), the NSTG composites exhibit the highest photodegradation efficiency. The apparent rate constant of NSTG is about 2.4 times and 50.7 times higher than that of NST and commercial TiO_2, respectively. Furthermore, the band gaps of the NSTG composites can be tuned by changing the molar ratio of citric acid (CA) : thiourea. Our work demonstrates that this innovative synthetic approach could provide an effective approach for industrial applications due to its low cost and scalability. Furthermore, the NSTG composites are a more promising photocatalytic material than the well studied N doped TiO_2 for potential applications in environmental protection.

Received 14th February 2017
Accepted 13th April 2017

DOI: 10.1039/c7ra01856h

rsc.li/rsc-advances

1. Introduction

Semiconductor photocatalysis is currently a prime research area because of its potential application in clean and renewable energy as well as pollution abatement.[1] In 1976, Fujishima *et al.* first reported that TiO_2 could be used as an electrode to decompose water under the condition of illumination.[2] This has opened up the prospect of TiO_2 in the field of photocatalysis. For over 40 years TiO_2 has been extensively studied and commonly applied as a photocatalyst in environmental cleaning and energy conversion because of its stability, oxidative power, nontoxicity, low cost, and efficiency for the degradation of complex organic pollutants.[3,4] However, photogenerated electrons and holes recombine quickly due to the wide band gap of TiO_2. Furthermore, this material only functions under UV light irradiation with a wavelength shorter than 387 nm, which only covers 4% of the solar spectrum.[5] The efficient use of sunlight has become an appealing challenge for photocatalyst development.

Due to efficient visible-light absorption by band gap modulation,[6] the promising and widely investigated systems are compounded semiconductor[7] and doped TiO_2, such as N doped TiO_2 (N-TiO_2), which show significant catalytic activity in various reactions under visible light irradiation.[8,9] Different strategies have been used for the doping of TiO_2. Asahi *et al.* first reported that nitrogen doping could narrow the band gap of TiO_2 and they synthesized N-TiO_2 *via* chemical treatments of the bare oxide.[10] Burda *et al.* prepared N-TiO_2 *via* sol–gel synthesis and reported enhanced visible light photocatalytic activity.[11] Other methods have been used for incorporating N in TiO_2, such as ion implantation and magnetron sputtering. Recently, NST has attracted much attention because of its synergistic effect which allows its electronic structure to be tuned and visible-light photocatalytic activity to be enhanced.[12] Herrera *et al.* reported enhanced photocatalytic activity for an NST which exhibited excellent catalytic activity under both

[a]*Department of Materials Science and Key Laboratory of Automobile Materials of MOE, Jilin University, Changchun, China. E-mail: tianhw@jlu.edu.cn*

[b]*The Second Hospital, Jilin University, Changchun, China*

[c]*State Key Laboratory of Automotive Simulation and Control, Jilin University, Changchun, China*

[d]*College of Science, Changchun University, Changchun, China*

[e]*Key Laboratory of Optical System Advanced Manufacturing Technology, Changchun Institute of Optics, Fine Mechanics and Physics, Chinese Academy of Sciences, Changchun, 130033, China*

† Electronic supplementary information (ESI) available: High-resolution TEM images of N, S-GQDs; Raman spectra of P25, NST and NSTG(1 : 1); high-resolution XPS of Ti 2p for NST and NSTG; XPS full survey spectra of N, S-GQDs, NST and NSTG(1 : 3) and PL spectra of P25, NST and NSTG(1 : 1) under UV-280 nm. See DOI: 10.1039/c7ra01856h

visible and UV light irradiation.[13] Xu and co-workers showed a twist-like helix NST with visible-light response.[14] Zhang *et al.* prepared N, S co-doped polymorphic TiO_2 which showed visible light photocatalytic activity for microcystin-LR degradation.[15] However, few studies have reported that the amount of dopant can have an on the band gap.

Although the application of two-dimensional graphene is unfortunately limited by its nature to easily aggregate and poor dispersion, graphene was further converted into 0D graphene quantum dots (GQDs) in 2007.[16,17] GQDs, which are only a few nanometers in size, have been recognised as a new type of quantum dots (QDs) with unique properties inherent from both graphene and QDs.[18] The characteristics of GQDs arises from their graphitic structure and quantum nature.[19,20] The strategies for synthesizing GQDs with tunable properties can be divided into two methods. One is the cutting approach in which graphene assemblies are directly cut into GQDs, such as nanolithography technique,[21] hydrothermal and solvothermal cutting of graphene[22] and electrochemical techniques.[23] The other is chemical synthesis by stepwise reactions of molecular precursors,[24] for example CA pyrolysis. Several reports showed promotion in the catalytic activity of GQDs, including the catalysis of GQDs,[25] enhanced photocatalytic activity under visible light,[26] and higher degradation efficiency of a TiO_2/GQDs composite compared with pure TiO_2 under visible light for the degradation of MB.[27] As carbon materials for catalysis, considerable efforts have been made to expand the diverse GQDs. For example, doped GQDs have been shown as an attractive channel to effectively tune intrinsic material properties since they possess electronic and optical characteristics, and surface and local chemical features. The N atom, which has similar atomic size as carbon atoms, has been widely applied in the elemental doping of carbon materials.[28,29] Sim *et al.* prepared N doped GQDs (N-GQDs) with electrocatalytic activity.[30] Dai *et al.* reported that N-GQDs/TiO_2 nanofibers present high photocurrents and excellent stability.[31] Recently, some researchers successfully synthesized co-doped GQDs, for example N, S co-doped GQDs (N, S-GQDs),[32] which reveal excellent catalytic activity and exhibit a narrower band gap than N-GQDs and thus absorption in the visible wavelength region.[33] However, co-doped GQDs based composites as photocatalysts have rarely been investigated for their degradation abilities for organic pollutants. Compared with the heavy metal semiconductor quantum dots used in photocatalysis, such as Cd^{2+} and W^{3+}, N, S-GQDs will not cause secondary pollution and also provide the excellent properties of semiconductor quantum dots.

Herein, for the first time, we synthesize NSTG composites with band tunability *via* a facile solvothermal treatment and report their enhanced photocatalytic activity through the degradation of MB. This synthetic method reduces the number of preparation steps without utilizing either excessively harmful reagents or unstable precursors and without generating particularly toxic by-products. We use CA as a carbon source to synthesize GQDs and thiourea as a precursor for the dopants. Commercial Degussa P25 is used as a precursor for TiO_2. Furthermore, the NSTG composites show continuously tunable band gaps by changing the molar ratio of CA : thiourea. The combination of NST and N, S-GQDs may improve charge separation and stabilization. The NSTG composites can effectively suppress electron–hole recombination, extend the range of visible light, and improve the catalytic efficiency. Therefore, this is an attractive and effective approach for industrial applications due to the significant reduction in economic cost and scalability.

2. Experimental

2.1 Materials

P25 (20% rutile and 80% anatase) was purchased from Degussa. CA and thiourea were supplied by Sinopharm Chemical Reagent Co., Ltd. (Shanghai, China). Ethanol (C_2H_6O) and dimethylformamide (DMF) were purchased from Beijing. Chemical Works (Beijing, China). All materials were used as received without further purification. Deionized (DI) water used in the preparation of the composites was obtained from local sources.

2.2 Synthesis

2.2.1 Synthesis of NSTG composites. CA and thiourea with different molar ratios of 1 : 0.5, 1 : 1, and 1 : 3 were dissolved in 8 mL DMF and stirred to form a clear solution.[34] Then 100 mg P25 was added to the solution and stirred to form a uniform suspension. Next, the suspension was transferred into a Teflon-lined stainless-steel autoclave. The solvothermal treatment was performed at 180 °C for 8 h. The products were cooled to room temperature and separated by centrifugation at 9000 rpm for 15 min after ethanol was added to the solution.

2.2.2 Synthesis of N, S-TiO_2 (NST). Thiourea was dissolved in 8 mL DMF and stirred to form a clear solution without the addition of CA. The rest of the steps were the same as that for the synthesis of the NSTG composites.

2.2.3 Synthesis of N, S-GQDs. CA and thiourea at a molar ratio of 1 : 3 were dissolved in 8 mL DMF and stirred to form a clear solution. Without the addition of P25, the rest of the steps were with the same as that for the synthesis of the NSTG composites.

2.3 Characterization

The as-prepared samples were characterized *via* XRD (Bruker, D8tools), SEM, (JOEL JSM-6700F), TEM, (JEM-2100F), Raman spectroscopy (Renishaw-1000), with 532 nm Ar laser excitation (a laser power of 7 mW), XPS, (Thermo ESCALAB 250 spectrometer), with a hemisphere detector (an energy resolution of 0.1 eV supplied by an Al Kα radiation source). UV-vis spectra were recorded using a Shimadzo UV-1601 PC spectrometer. FT-IR spectra were collected using a Biorad FTS-60A FTIR device equipped with a diffuse reflectance unit. The visible light was supplied by a 300 W Xe arc lamp (PLS-SXE 300, Beijing Perfect Light Co., Ltd.).

2.4 Photocatalytic activity test

The photocatalytic activity of the samples was evaluated through the degradation of MB in aqueous solution under visible light from a 300 W Xe arc lamp with a UV-CUT filter to

cut off light of wavelength <400 nm. 20 mg of sample was added to 80 mL of MB solution (10 ppm). Prior to irradiation, the photocatalysts were not subjected to any treatment and were dispersed in MB solution under magnetic stirring in the dark for 30 min to ensure the establishment of adsorption/desorption equilibrium. Afterward, the solution was exposed to visible light irradiation. After a specific time interval (1 h), 4 mL solution was sampled and subjected to centrifugation to separate the catalyst. The MB concentration was monitored by the absorbance value at the maximum peak using a UV-vis scanning spectrophotometer.

3. Results and discussion

Fig. 1 shows the XRD patterns of P25, NST, NSTG(1 : 0.5), NSTG(1 : 1), and NSTG(1 : 3). NSTG with different weight ratios of thiourea and NST display a typical anatase phase with diffraction peaks corresponding to the (101), (004), (200), (105), (211), (204), (116), (220) and (215) crystal planes,[35] whereas the rutile phase typically exhibits diffraction peaks corresponding to the (110) and (101) planes. No diffraction peaks of carbon species are observed in these composites when N, S-GQDs are added to them, which is due to the small amount and weak intensity of the GQDs. Furthermore, it is possible that the main graphene peak is shielded by the peak of anatase TiO_2. From the inset XRD pattern, the (101) peak for NST shifts left to smaller angles compared with P25, which is attributed to the increase in crystal spacing. Furthermore, with an increase in thiourea the (101) peaks for all the samples gradually broaden. The broadening of the diffraction peaks is indicative of the small size of the obtained nanoparticles. These results indicate that the lattice structure of is distorted by the interaction with the dopants.[36] To clarify the effect of thiourea on the lattice structure of TiO_2, the lattice parameters of TiO_2 were measured using (101) and (200) in the anatase crystal planes using Bragg's equation and interplanar spacing formula. As shown in Table 1 (ESI†), it is clear that the lattice parameters of all the TiO_2 samples remain almost unchanged along the *a* and *b* axes, whereas the *c* axis parameter changes due to the presence of adventitious N and S. The lattice parameter increases, which leads to an increase in the crystal plane spacing.[37] However, it can be seen that nitrogen and sulfur doping does not significantly change the size of the particles and the crystal structure of the samples.

The Raman shift peaks (Fig. S1, ESI†) at 144 cm^{-1} (E_g), 398 cm^{-1} (B_{1g}), 517 cm^{-1} (A_{1g}), and 638 cm^{-1} (E_g) correspond to the characteristic peaks of the anatase phase.[38] The peak shift and broadening of the Raman spectra were analyzed using the most intense peak which was at 144 cm^{-1} (E_g). The peak position and broadening of the Raman spectrum are mainly affected by the size of the nanomaterial as well as defects and temperature.[39] As seen in the inset of Fig. S1,† the main anatase Raman band at the peak position of about 144 cm^{-1} was sharpened and blue-shifted when nitrogen and sulfur were doped into the lattice of TiO_2. The blue shift is due to the decrease in the size of the sample. According to previous reports, nitrogen easily replaces oxygen and S^{6+} easily replaces Ti^{4+} in the lattice of TiO_2.[40] Furthermore, the ionic radius of N^{3-} is similar with that of O^{2-}. The ionic radius of S^{6+} is less than that of Ti^{4+}.[41] Above all, the size confinement effect is believed to be mainly responsible for the Raman band shift. The results indicate that nitrogen and sulfur were doped into the lattice of TiO_2 successfully.

Fig. 2A shows the SEM image of the NSTG composite, in which the nanoparticles intertwine with each other to form a porous spherical morphology due to the formation of TiO_2 clusters. Due to the solvothermal reaction, the generated N, S-GQDs and NST combine with each other because of intermolecular forces. The N, S-GQDs are attached on the surface of NST. However, due to the small particle size of the GQDs, a clear

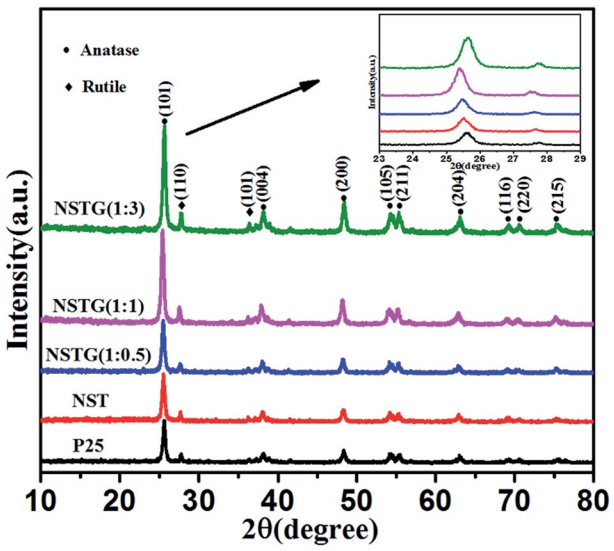

Fig. 1 XRD patterns of P25, NST, NSTG(1 : 0.5), NSTG(1 : 1), and NSTG(1 : 3). Inset XRD pattern shows the 23–29 degree region.

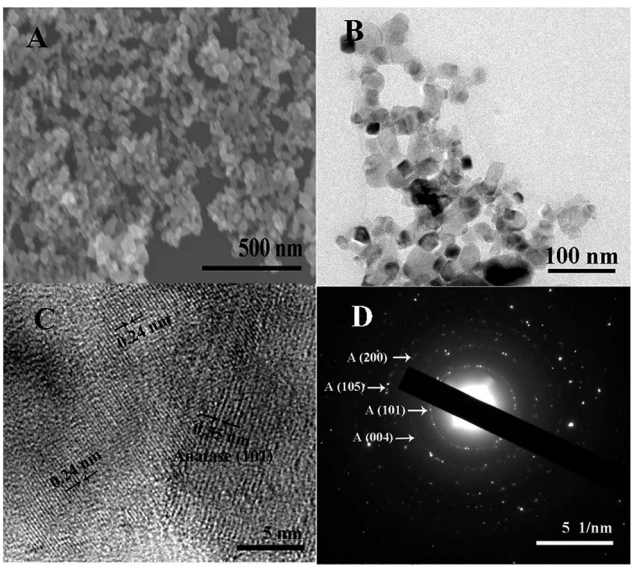

Fig. 2 (A) SEM, (B) TEM and (C) high-resolution TEM images of the NSTG(1 : 1) composite. (D) Corresponding selected area electron diffraction pattern.

observation using SEM could not be achieved. The TEM image of the obtained NSTG displays its microstructure, as shown in Fig. 2B. It consists of intergrown fundamental particles with a rough and uneven surface. As estimated from the TEM image, the average size of the nanoparticles is about 10 nm. It can be seen that the TiO_2 nanoparticles occupy most of the available surface area which provides a high loading of GQDs in the composites. As shown in Fig. 2C, the HRTEM image shows the lattice fringes of NSTG with an interplanar spacing of 0.35 nm and 0.24 nm, which correspond to TiO_2 (101) and N, S-GQDs (1120), respectively. The high-resolution TEM image (Fig. S2, ESI†) reveals that the lattice spacing of 0.24 nm corresponds to N, S-GQDs (1120), which demonstrates the existence of N, S-GQDs. The selected area electron diffraction (SAED) pattern of the NSTG composite shown in Fig. 2D clearly presents concentric diffraction rings which match well with the (101), (004), (200), and (105) planes of the anatase TiO_2 phase. The high intense (101) feature highlights that the TiO_2 crystallites are preferentially oriented along the (101) plane.

The bonding of nitrogen and sulfur in NST and NSTG was examined by FT-IR measurements. Fig. 3 shows the FT-IR spectra of the samples in the range of 4000 to 500 cm^{-1}. The strong absorption peak at about 3400 cm^{-1} is an extension of adsorbed water and the small peak at 1633 cm^{-1} is associated with the C=O stretching vibrations of the COOH groups. The strong intensity of the peaks at 3400 and 1633 cm^{-1} indicates a high content of adsorbed water and hydroxyls in the sample. Furthermore, the adsorbed water and hydroxyls would be beneficial for the photocatalytic activity of the catalysts. The greater the number of surface hydroxyl groups, the faster the photocatalytic reaction.[42] The FT-IR spectra show the main bands at 500–700 cm^{-1}, which are attributed to the Ti–O stretching and Ti–O–Ti stretching vibrations. The absorption peaks presented in the spectra of NST and NSTG at about 1405 cm^{-1} are attributed to the adsorption of SO_4^{2-} with bidentate bonds. In the spectrum of NST, the absorption peaks at 1131 cm^{-1} and 1045 cm^{-1} are assigned to the Ti–O–S bond and Ti–S bond, respectively. The weak band at 1410 cm^{-1} is ascribed to the bonding vibration of NH^{4+}. Furthermore, the stretching vibrations of C–N are detected at 1101 cm^{-1}. The bands at 1715 and 1655 cm^{-1} are attributed to the vibrational absorption bond of C=O in COOH and CONH, respectively. The stretching vibration of N–H shows a broad absorption at 3000–3500 cm^{-1}. This indicates the presence of amino groups on the surface of GQDs, which results in GQDs with good hydrophilic properties. In the FT-IR spectra of the NSTG composites, the peak at about 2100 cm^{-1} is due to C≡N which occurs during the synthesis of N, S-GQDs and is evidence that the N, S-GQDs were synthesized during the solvothermal treatment.

XPS analysis was performed in order to identify the chemical state of the N and S elements in the samples. The high-resolution N 1s XPS spectra of NST are shown in Fig. 4A. As seen from the N 1s of NST, two peaks are found at around 399.7 and 401.1 eV. The main peak at 399.7 eV is attributed to the presence of substitutional nitrogen as a characteristic of O–Ti–N, which indicates that some of the lattice oxygen was substituted by N atoms.[43] The peak at 401.1 eV can be assigned to interstitial N-doping and/or the formation of Ti–O–N species. Compared with the N 1s of NSTG in Fig. 4C, the O–Ti–N and Ti–O–N species have slight deviation. This is mainly because N, S-GQDs are combined with NST. The N 1s of NSTG shows two extra peaks at 399.2 and 400.3 eV, which are attributed to the pyrrolic N (C–N–C) and graphitic N or N–H bands, respectively. All of the above results confirm that N is not only successfully implanted in the structure but is also present in a chemically bonded state. Fig. 4B shows the corresponding high-resolution S 2p XPS spectra of NST. The S 2p XPS peaks centered at 168.7 and 169.6 eV for the NST sample could be attributed to S^{6+}

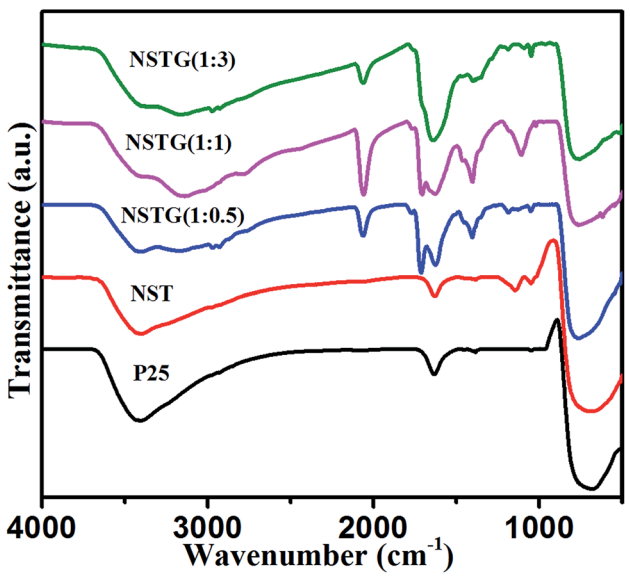

Fig. 3 FT-IR spectra of the P25, NST, NSTG(1 : 0.5), NSTG(1 : 1) and NSTG(1 : 3) samples.

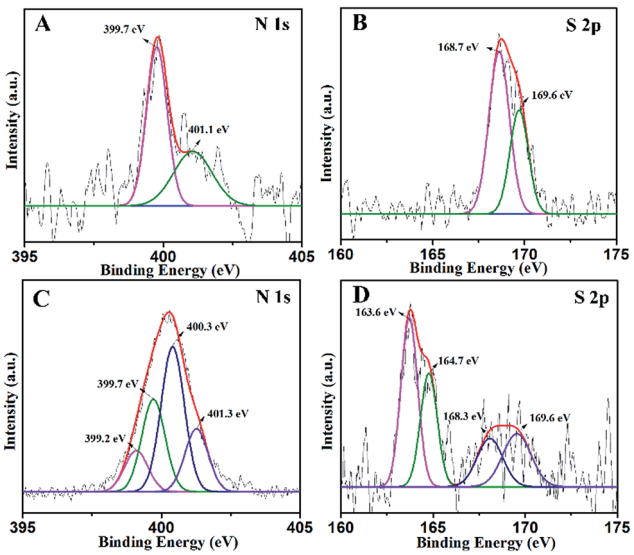

Fig. 4 High-resolution N 1s XPS spectra of (A) NST and (C) NSTG(1 : 3) and S 2p of (B) NST and (D) NSTG(1 : 3).

species, which correspond to the S^{6+} cation in the S=O and S–O bonds formed when some of the Ti^{4+} in the TiO_2 lattice are replaced by sulfur atoms. In the S 2p spectra of the NSTG composite shown in Fig. 4D, the two clear peaks at 163.6 and 164.7 eV represent S $2p_{3/2}$ and S $2p_{1/2}$ of thiophene, respectively. The two other peaks at 168.3 and 169.6 eV correspond to S=O in NST and N, S-GQDs, respectively, which shift negatively because sulfur doping with GQDs and TiO_2 needs a higher formation energy than single doping with TiO_2.[44] However, it is noted that there is no signal for anionic S species in the composite because replacing O^{2-} with S^{2-} requires a higher formation energy. These results indirectly indicate that the NSTG composites have been successfully synthesized *via* our approach. The XPS spectral peaks for Ti 2p of NST and NSTG (Fig. S3A, ESI†) at 459.1 and 464.8 eV are attributed to the binding energies of the Ti $2p_{3/2}$ and $2p_{1/2}$ electrons, respectively. Fig. S3B† displays the full XPS survey spectra of N, S-GQDs, NST and NSTG. The prepared samples contain Ti, O, C, N and S with the binding energies corresponding to Ti 2p, O 1s, C 1s, N 1s and S 2p, respectively. The peaks at 169.2, 284.8, 400.1, 458.3 and 533.4 eV correspond to S 2p, C 1s, N 1s Ti 2p and O 1s, respectively. This indicates that the as prepared GQDs and TiO_2 are doped with N and S atoms.

As shown in Fig. 5A, the UV-vis spectrum of the as-prepared N, S-GQDs reveals absorption bands located at 391, 464, 550 and 652 nm. The origin of these peaks is related to the electron transition in the heteroatom-containing GQDs. The absorption peak at 391 nm corresponds to the n → π* transition of the conjugated C=O and C=N bonds.[45] The absorption peak at 464 nm is due to the n → π* transition of the conjugated C=N and C=S bonds, the absorption peak at 550 nm is attributed to the n → π* transition of the conjugated C=S bond and the absorption peak at 652 nm is ascribed to the n → π* transition of the conjugated S=O bond.[34] It is obvious that the N, S-GQDs have a wide absorption range for visible light. As shown in the inset of Fig. 5A from left to right, the N, S-GQDs exhibit different colors under 254, 302 and 365 nm visible light irradiation, which is attributed to their conjugated structure, quantum size effect, surface state, edge effect, carbon nuclear state and molecular state. This indirectly indicates that N, S-GQDs were synthesized in the solvothermal treatment.

The UV-vis absorption spectra of P25, NST and NSTG with dopant ratios are shown in Fig. 5B. There is an obvious red shift from 392 to 468 nm for the absorption edge with an increase in the amount of thiourea. A remarkable red shift in the absorption edge to the visible light region is observed for NST compared with P25. This result indicates that the lattice distortion of TiO_2 is responsible for the red-shift absorption band of NST. Moreover, it demonstrates that doping can tune the band gap of TiO_2 to reduce the energy required for photoactivation.[46] With the increase in dopant concentration, an obvious red shift in the absorption edge of NSTG can be observed in comparison to NST. This indicates that the band gap of the NSTG composites is narrower than NST. The remarkable red shift may be ascribed to the synergetic effect between NST and N, S-GQDs. The band gap energy of the samples could be calculated by applying the Kubelka–Munk formula,[47] and the corresponding $(ahv)^{1/2}$ photon

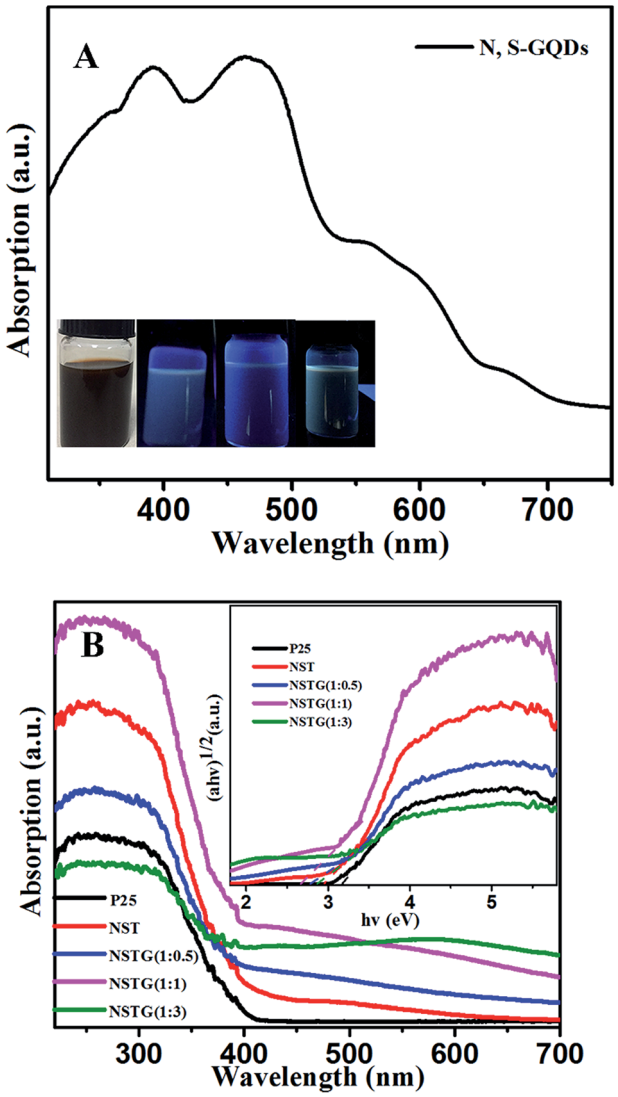

Fig. 5 (A) UV-vis absorption spectrum of N, S-GQDs and inset shows images of the different colors of N, S-GQD. (B) UV-vis absorption spectra of P25, NST, NSTG(1 : 0.5), NSTG(1 : 1), and NSTG(1 : 3). The inset is the estimated band gap from the Kubelka–Munk function.

energy is shown in the inset of Fig. 5B, where *a*, *h*, and *v* correspond to the absorption coefficient, Planck's constant, and frequency, respectively. It is obvious that the band gap of the NSTG composites can be well tuned by changing the molar ratio of CA : thiourea during the solvothermal synthesis. From the calculations, the band gaps of P25, NST, NSTG(1 : 0.5), NSTG(1 : 1), and NSTG(1 : 3) are estimated to be about 3.16, 2.93, 2.78, 2.65 and 2.85 eV, according to the absorption edges at about 392, 423, 446, 468 and 435 nm, respectively. The narrowing of the band gap of NST is due to the contributions of both doping atoms and oxygen vacancies in the lattice. The doping atoms induce local states above the valence band edge and the oxygen vacancies give rise to local states consisting of the 3d states of Ti^{3+} below the conduction band edge.[43] Furthermore, the narrowing of the band gap of NSTG could be chiefly attributed to the synergetic absorption effect of combining with N, S-GQDs, which

have a narrow band gap, and formation of chemical bonding through co-doping with N and S.

XPS spectra not only give information on the binding energy of a specific element but also the total density of states (DOS) of the valence band (VB). More information about the VB of samples can be obtained *via* VB XPS. The DOS of the VB is presented in Fig. 6. P25 displays VB DOS in Fig. 6A, with the edge of the maximum energy at about 3.04 eV. According to Fig. 5B, the band gap of P25 is 3.16 eV. Thus, the conduction band (CB) minimum should be present at about −0.12 eV by calculation.[48] The DOS of the VB in NST, NSTG(1 : 0.5), NSTG(1 : 1), and NSTG(1 : 3) with the edge of the maximum energy are at about 2.80, 2.56, 2.41 and 2.66 eV, and their CB are calculated to be about −0.13, −0.22, −0.24, and −0.19 eV, respectively, as shown in Scheme 1. For NSTG, its VB maximum energy blue-shifts compared with NST. From the DOS of the valence bands (VBs) of these samples, the VBs really change due to the doping. Combined with the results from the UV-vis absorption spectra, which suggest a much narrowed band gap, the CB of the NSTG composites substantially change. This is evidence that the band gap of nanomaterial we synthesized is indeed narrowed. The N, S-GQDs present the VB DOS with the edge of the maximum energy at about −0.43 eV. It could promote electronic transition and produce active oxygen (˙O2) and hydroxyl (˙OH) radicals. The band gap of graphene is 0.

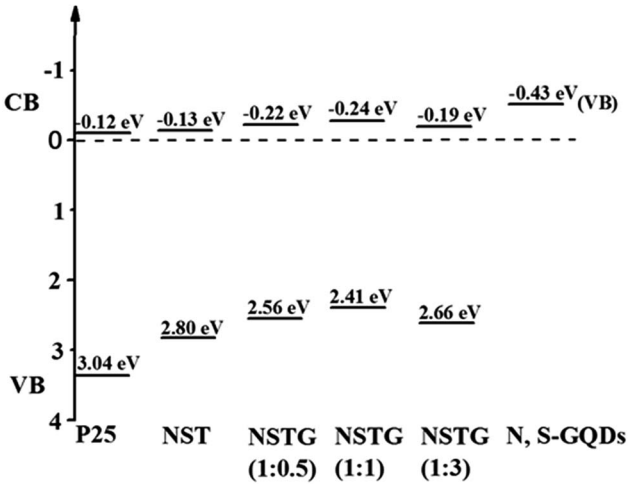

Scheme 1 Schematic illustration of the DOS of P25, NST, NSTG(1 : 0.5), NSTG(1 : 1), NSTG(1 : 3), and N, S-GQDs.

Thus, this is evidence that N, S-GQDs were generated during our solvothermal method.

According to the photoluminescence (PL) emission spectra, we can investigate the electronic structure, and optical and photochemical properties of the active sites on the surface of the catalysts to determine the lifetime of the electron–hole pairs because the PL emission results from the recombination of free charge carriers. The PL spectra for P25, NST and NSTG (Fig. S4, ESI†) use the excitation light of 280 nm UV light. It is obvious that the PL intensity of P25 is higher than NST, which indicates that N and S doping can effectively inhibit excited electron and hole recombination. There are two steps in the process of electron and hole recombination: first, the hydroxyl groups of TiO_2 are trapped by holes to form hydroxyl radicals which can suppress electron–hole recombination due to the doping.[49] Second, theoretical and experimental investigation indicates that nitrogen and sulfur doping results in the easy formation of oxygen vacancies. Thus, electrons are trapped by the oxygen vacancies, whereas holes are trapped by the doped N and S atoms, which decreases the PL intensity.[50] The PL intensity of NST is higher than NSTG, which indicates that the N, S-GQDs are compounded with NST effectively. Thus, the NSTG composites can extend their absorption response more than NST, which increases the efficiency of electronic transition. Finally, this successfully reduces the probability of electron–hole recombination.

The photocatalytic activity of the prepared samples was investigated *via* the degradation of MB under visible light (λ > 400 nm). The self-photodegradation of MB in the absence of photocatalyst is negligible. The normalized temporal concentration changes (C_t/C_0) of MO during the photodegradation are proportional to the normalized maximum absorbance (A_t/A_0) and derived from the changes in the absorption profile of the dye at a given time interval.[51]

As shown in Fig. 7, almost no photocatalytic activity is observed for the P25 catalyst under visible light irradiation and only 8% of the MB diminished after 4 h. However, it can be

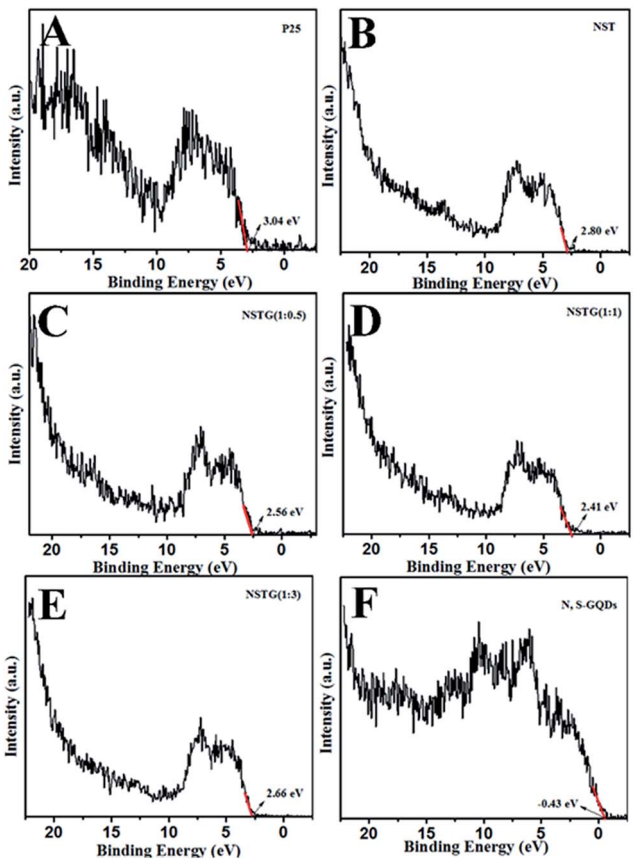

Fig. 6 VB XPS spectra of (A) P25, (B) NST, (C) NSTG(1 : 0.5), (D) NSTG(1 : 1), (E) NSTG(1 : 3), and (F) N, S-GQDs.

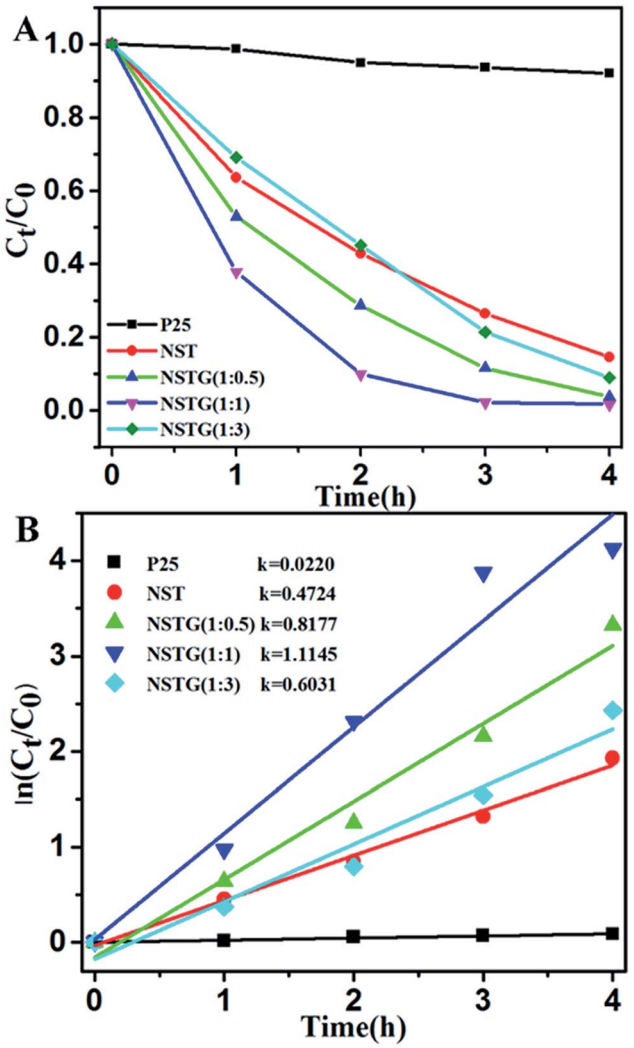

Fig. 7 (A) Photocatalytic activities and (B) linear fittings of the pseudo-first order kinetics model for the degradation of methylene blue (MB) under visible light (λ > 400 nm) irradiation for the different catalysts: P25, NST, NSTG(1 : 0.5), NSTG(1 : 1) and NSTG(1 : 3).

seen that the NST prepared by solvothermal treatment exhibits higher visible light photocatalytic activity than P25. The photodegradation efficiency of NST which is about 85.5% is 14.2 times that of P25. Through compounding with N, S-GQDs, the composites display significant improvements for the photodegradation of MB compared to P25 and NST. With the increase in dopant content, the photocatalytic activity of NSTG first increases and then decreases. When the molar ratio of CA : thiourea is 1 : 1, NSTG(1 : 1) exhibits the highest photocatalytic activity. The blue color of the MB solution fades completely upon visible light irradiation. The photodegradation efficiency of NSTG(1 : 1) which is about 98.4% is 1.2 and 16.4 times that of NST and P25, respectively. The photodegradation rate of MB generally follows a pseudo-first-order kinetic process, which can be expressed by the equation $\ln(C_t/C_0) = k \times t$, where k, C_0 and C_t are the apparent rate constant, initial MB concentration and MB concentration after a certain time, respectively.

The calculated reaction rate constants of MB degradation under visible light irradiation are 0.0220, 0.4724, 0.8177, 1.1145 and 0.6031 h^{-1} for P25, NST, NSTG(1 : 0.5), NSTG(1 : 1) and NSTG(1 : 3), respectively (as shown in Fig. 7B). The apparent reaction rate constant of NSTG(1 : 1), which has the highest activity, is 2.4 and 50.7 times higher than that of NST and P25, respectively. As shown above, co-doping can reduce the band gap of TiO_2 and increase absorption in the visible region, which provide NSTG with efficient visible light photocatalytic activity. The excellent degradation ability of NSTG is due to the broad absorption band from N, S-GQDs starting from 300 to 750 nm. This is also the reason why the NSTG composite exhibits a higher photocatalytic performance in comparison to P25 and NST. However, NSTG(1 : 3) with a higher nitrogen and sulfur content exhibits lower activity because the higher nitrogen and sulfur content results in the production of more oxygen vacancies.[52] These oxygen vacancies populate the impurity states and thus suppress the photocatalytic activity.[53] The synthesized NSTG(1 : 1) possesses the maximum photocatalytic activity, which suggests that there is an optimum value for co-doping.

The photodegradation efficiency can be expressed by the equation $R = (C_0 - C_t)/C_0 \times 100\%$, where C_0 and C_t are the initial MB concentration and MB concentration after a certain time, respectively. According to the results, NSTG(1 : 1) possesses the highest photocatalytic activity; thus, it was utilized repeatedly four times to photodegradate MB in four hours. As shown in Fig. 8, a 3% decrease in photodegradation efficiency was observed after four consecutive runs under visible light irradiation, which indicates the excellent photocatalytic stability of the photocatalyst for the treatment of organic pollutants in wastewater. The slight deactivation the catalyst upon recycling may be a result of the accumulation of intermediates, such as carbonates, formed during the degradation process.

The distribution curves of the VB and CB are exhibited in Scheme 1. With an increase the amount of thiourea, the VBs of

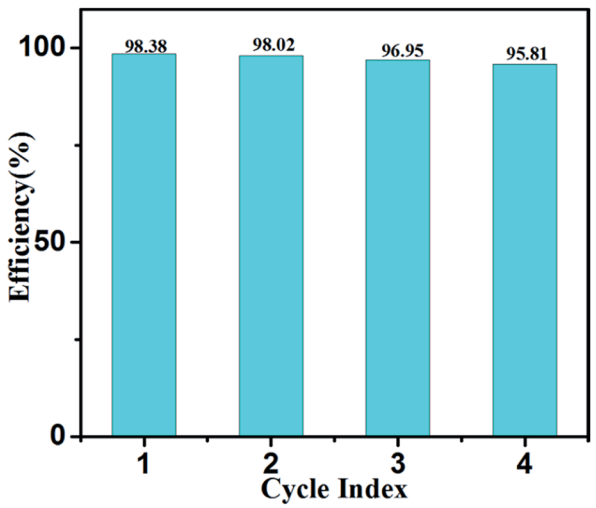

Fig. 8 MB photodegradation activity measured with the recycled catalysts (1–4 cycles, time = 4 h).

the samples generally decrease first and then increase. Therefore, the conduction bands (CBs) maintain a consistent changing trend. This is due to the synergistic effect of co-doping and N, S-GQDs with a VB at about −0.43 eV.[54] Although GQDs are not semiconductor, N, S-GQDs have the properties of semiconductor due to the quantum effect and co-doping.[55] Their VB is higher and more conducive to electronic transition, thus more electrons and holes are produced. The possible photocatalytic degradation mechanism of NSTG is illustrated in Scheme 2. There are two possible pathways to generate active species for MB degradation under visible light in NSTG. The enhanced photocatalytic activity of NSTG is due to the synergism between N, S-GQDs and NST. First, the large aromatic structure of the GQDs creates high affinity for MB. In addition, the large surface area of the GQDs also increases the adsorption of MB. As a co-catalyst, the N, S-GQDs not only absorb visible light efficiently but also act as a photosensitizer due to their broad visible light absorption under visible light irradiation. Thus, electrons in the VB of N, S-GQDs can be excited to the CB and then electron–hole pairs are generated.[56] The electrons excited are injected into NST because the N, S-GQDs attach onto the surface of NST. This process is accompanied by charge separation. Second, due to the N and S co-doping, the significant band broadening and red-shift in the UV-visible absorption spectrum of NST suggests a band gap reduction compared with that of P25. The co-doping of N and S into the crystal lattice of TiO_2 alters the electronic band structure of TiO_2. The electrons of NST can be excited directly into the TiO_2 CB under visible light irradiation. Then, electron–hole pairs are generated as well. These charge separation processes in the two pathways promote the formation of active oxygen ($^{\bullet}O_2$) and hydroxyl ($^{\bullet}OH$) radicals. MB is adsorbed on the surface of the catalyst and oxidized indirectly through the hydroxyl radicals ($^{\bullet}OH$) generated by the reaction of holes and the superoxide radicals ($^{\bullet}O_2$) produced by the photogenerated electrons.[57] The $^{\bullet}O_2$ radical plays an important role because of strong oxidation in the degradation of MB. After a series of reactions, MB molecules are finally degraded into CO_2 and H_2O. The synergistic effects of increasing visible light absorption and fast transferring of charge carriers to the surfaces are responsible for the high visible light photocatalytic activity of NSTG.

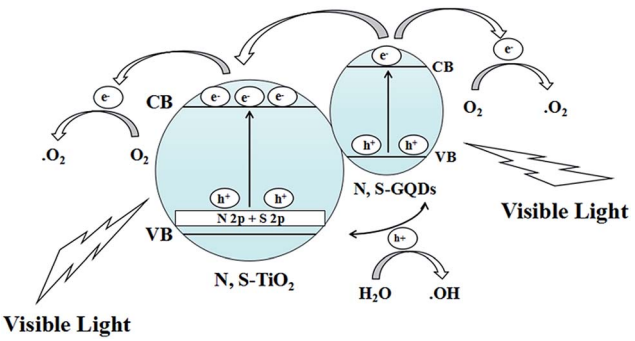

Scheme 2 Possible photocatalytic mechanism for NSTG under visible light irradiation.

4. Conclusions

In summary, we prepared NSTG composites with band tunability *via* a one step facile solvothermal treatment process. These composites simultaneously exhibit an extended photoresponse range, and enhanced charge separation and transportation properties. Based on their superior material properties, the NSTG composites demonstrate significant advancements over P25 and NST for the photodegradation of MB under visible light irradiation. The apparent rate constant of NSTG(1 : 1) is 2.4 and 50.7 times higher than that of NST and P25, respectively. The enhanced photocatalytic activity is due to the synergistic effects between N, S-GQDs and NST, including the optimal band gap and moderate CB position for NSTG, efficient separation and transfer ability of the photogenerated electron–hole pairs. This work not only indicates that NSTG is highly suitable as a visible light driven photocatalyst for the degradation of organic pollutants, but also provides an innovative approach which is a green, facile and economical method to synthesize co-doped TiO_2/co-doped GQDs composites with high photocatalytic activity for efficient solar energy utilization.

Acknowledgements

Financial support from the National Natural Science Foundation of China (No. 51472106 and 51372095) and the Key Project of Science and Technology of The Jilin Provincial Education Department during the 13th Five-Year Plan Period are highly appreciated.

Notes and references

1 M. R. Hoffmann, S. T. Martin, W. Y. Choi and D. W. Bahnemann, *Chem. Rev.*, 1995, **95**, 69–96.
2 A. Fujishima and K. Honda, *Nature*, 1972, **238**, 37–38.
3 C. Xue, X. Xu, G. Yang and S. Ding, *RSC Adv.*, 2015, **5**, 102228–102237.
4 L. Bai, F. Fang, Y. Zhao, Y. Liu, J. Li, G. Huang and H. Sun, *RSC Adv.*, 2014, **4**, 43039–43046.
5 X. Chen and S. S. Mao, *Chem. Rev.*, 2007, **107**, 2891–2959.
6 Y. Wang, H. Lu, Y. Wang, J. Qiu, J. Wen, K. Zhou, L. Chen, G. Song and J. Yao, *RSC Adv.*, 2016, **6**, 1860–1864.
7 J. Qiu, Y. Feng, X. Zhang, X. Zhang, M. Jia and J. Yao, *RSC Adv.*, 2017, **7**, 10668–10674.
8 L. Li, B. Wu, G. Li and Y. Li, *RSC Adv.*, 2016, **6**, 28904–28911.
9 H. Li, Y. Hao, H. Lu, L. Liang, Y. Wang, J. Qiu, X. Shi, Y. Wang and J. Yao, *Appl. Surf. Sci.*, 2015, **344**, 112–118.
10 R. Asahi, T. Morikawa, T. Ohwaki, K. Aoki and Y. Taga, *Science*, 2001, **293**, 269–271.
11 C. Burda, Y. B. Lou, X. B. Chen, A. C. S. Samia, J. Stout and J. L. Gole, *Nano Lett.*, 2003, **3**, 1049–1051.
12 M. Sathish, R. P. Viswanath and C. S. Gopinath, *J. Nanosci. Nanotechnol.*, 2009, **9**, 423–432.
13 J. A. Rengifo-Herrera, K. Pierzchała, A. Sienkiewicz, L. Forró, J. Kiwi and C. Pulgarin, *Appl. Catal., B*, 2009, **88**, 398–406.
14 J. H. Xu, J. Li, W. L. Dai, Y. Cao, H. Li and K. Fan, *Appl. Catal., B*, 2008, **79**, 72–80.

15 G. Zhang, C. Z. Yong, M. Nadagouda, C. Han, K. O'Shea, S. M. El-Sheikh, A. A. Ismail and D. D. Dionysiou, *Appl. Catal., B*, 2014, **144**, 614–621.
16 B. Trauzettel, D. V. Bulaev, D. Loss and G. Burkard, *Nat. Phys.*, 2007, **3**, 192–196.
17 J. M. Pereira, P. Vasilopoulos and F. M. Peeters, *Nano Lett.*, 2007, **7**, 946–949.
18 Z. Zhang, J. Zhang, N. Chen and L. Qu, *Energy Environ. Sci.*, 2012, **5**, 8869.
19 A. Kelarakis, *Curr. Opin. Colloid Interface Sci.*, 2015, **20**, 354–361.
20 N. Maity, A. Kuila, S. Das, D. Mandal, A. Shit and A. K. Nandi, *J. Mater. Chem. A*, 2015, **3**, 20736–20748.
21 L. A. Ponomarenko, F. Schedin, M. I. Katsnelson, R. Yang, E. W. Hill, K. S. Novoselov and A. K. Geim, *Science*, 2008, **320**, 356–358.
22 D. Pan, J. Zhang, Z. Li and M. Wu, *Adv. Mater.*, 2010, **22**, 734–738.
23 L. Zheng, Y. Chi, Y. Dong, J. Lin and B. Wang, *J. Am. Chem. Soc.*, 2009, **131**, 4564–4565.
24 Y. Dong, J. Shao, C. Chen, H. Li, R. Wang, Y. Chi, X. Lin and G. Chen, *Carbon*, 2012, **50**, 4738–4743.
25 J. Shen, Y. Zhu, X. Yang and C. Li, *Chem. Commun.*, 2012, **48**, 3686–3699.
26 S. Liu, Q. Lu and Y. Zhang, *J. Mater. Chem. A*, 2015, **3**, 8552–8558.
27 D. Tan, S. Zhou and J. Qiu, *ACS Nano*, 2012, **6**, 1059–1064.
28 Y. Du and S. Guo, *Nanoscale*, 2016, **8**, 2532–2543.
29 F. Lou, M. E. M. Buan, N. Muthuswamy, J. C. Walmsley, M. Ronning and D. Chen, *J. Mater. Chem. A*, 2015, **4**, 1233–1243.
30 U. Sim, J. Moon, J. An, J. H. Kang, S. E. Jerng, J. Moon, S. P. Cho, B. H. Hong and K. T. Nam, *Energy Environ. Sci.*, 2015, **8**, 1329–1338.
31 Y. Dai, H. Long, X. Wang, Y. Wang, Q. Gu, W. Jiang, Y. Wang, C. Li, T. H. Zeng and Y. Sun, *Part. Part. Syst. Charact.*, 2014, **31**, 597–604.
32 Z. Luo, D. Yang, G. Qi, J. Shang, H. Yang, Y. Wang, L. Yuwen, T. Yu, W. Huang and L. Wang, *J. Mater. Chem. A*, 2014, **2**, 20605–20611.
33 D. Qu, M. Zheng, P. Du, Y. Zhou, L. Zhang, D. Li, H. Tan, Z. Zhao, Z. Xie and Z. Sun, *Nanoscale*, 2013, **5**, 12272–12277.
34 D. Qu, Z. Sun, M. Zheng, J. Li, Y. Zhang, G. Zhang, H. Zhao, X. Liu and Z. Xie, *Adv. Opt. Mater.*, 2015, **3**, 360–367.
35 S. D. Perera, R. G. Mariano, K. Vu, N. Nour, O. Seitz, Y. Chabal and K. J. Balkus, *ACS Catal.*, 2012, **2**, 949–956.
36 B. Naik, K. M. Parida and C. S. Gopinath, *J. Phys. Chem. C*, 2010, **114**, 19473–19482.
37 L. Turner-Stokes, N. Sykes, E. Silber and G. D. Group, *Bull. Korean Chem. Soc.*, 2008, **29**, 1217–1223.
38 F. Dong, H. Wang and Z. Wu, *J. Phys. Chem. C*, 2009, **113**, 16717–16723.
39 H. Tian, C. Wan, W. Zheng, X. Hu, L. Qiao and X. Wang, *RSC Adv.*, 2016, **6**, 84722–84729.
40 Q. Xiang, J. Yu and M. Jaroniec, *Phys. Chem. Chem. Phys.*, 2011, **13**, 4853–4861.
41 M. Rahm, R. Hoffmann and N. W. Ashcroft, *Chem.–Eur. J.*, 2016, **22**, 14625–14632.
42 D. H. Wang, L. Jia, X. L. Wu, L. Q. Lu and A. W. Xu, *Nanoscale*, 2012, **4**, 576–584.
43 S. Livraghi, M. C. Paganini, E. Giamello, A. Selloni, V. C. Di and G. Pacchioni, *J. Am. Chem. Soc.*, 2006, **128**, 15666–15671.
44 C. Y. Jimmy, H. Wingkei, Y. Jiaguo, Y. Hoyin, P. Keung Wong and J. Zhao, *Environ. Sci. Technol.*, 2005, **39**, 1175–1179.
45 T. F. Yeh, C. Y. Teng, S. J. Chen and H. Teng, *Adv. Mater.*, 2014, **26**, 3297–3303.
46 F. Dong, W. Zhao and Z. Wu, *Nanotechnology*, 2008, **19**, 2618–2624.
47 F. Spadavecchia, G. Cappelletti, S. Ardizzone, C. L. Bianchi, S. Cappelli, C. Oliva, P. Scardi, M. Leoni and P. Fermo, *Appl. Catal., B*, 2010, **96**, 314–322.
48 X. Chen, L. Liu, P. Y. Yu and S. S. Mao, *Science*, 2011, **331**, 746–750.
49 K. Nagaveni, M. S. Hegde, N. Ravishankar, G. N. Subbanna and G. Madras, *Langmuir*, 2004, **20**, 2900–2907.
50 L. Jing, X. Sun, W. Cai, Z. Xu, Y. Du and H. Fu, *J. Phys. Chem. Solids*, 2003, **64**, 615–623.
51 A. Houas, H. Lachheb, M. Ksibi, E. Elaloui, C. Guillard and J. M. Herrmann, *Appl. Catal., B*, 2001, **31**, 145–157.
52 C. D. Valentin, G. Pacchioni and A. Selloni, *Chem. Mater.*, 2005, **17**, 6656–6665.
53 H. Kamisaka, T. Adachi and K. Yamashita, *J. Chem. Phys.*, 2005, **123**, 084704.
54 M. A. Sk, A. Ananthanarayanan, L. Huang, K. H. Lim and P. Chen, *J. Mater. Chem. C*, 2014, **2**, 6954–6960.
55 S. Yang, J. Sun, X. Li, W. Zhou, Z. Wang, P. He, G. Ding, X. Xie, Z. Kang and M. Jiang, *J. Mater. Chem. A*, 2014, **2**, 8660–8667.
56 R. Zhang, S. Qi, J. Jia, B. Torre, H. Zeng, H. Wu and X. Xu, *J. Alloys Compd.*, 2015, **623**, 186–191.
57 H. Tian, K. Shen, X. Hu, L. Qiao and W. Zheng, *J. Alloys Compd.*, 2016, **691**, 369–377.